The Medipix3RX: a high resolution, zero dead-time pixel detector readout chip allowing spectroscopic imaging

2013 JINST 8 C02016

(http://iopscience.iop.org/1748-0221/8/02/C02016)

PUBLISHED BY IOP PUBLISHING FOR SISSA MEDIALAB

RECEIVED: *September 30, 2012*
ACCEPTED: *December 27, 2012*
PUBLISHED: *February 8, 2013*

14th INTERNATIONAL WORKSHOP ON RADIATION IMAGING DETECTORS,
1–5 JULY 2012,
FIGUEIRA DA FOZ, PORTUGAL

The Medipix3RX: a high resolution, zero dead-time pixel detector readout chip allowing spectroscopic imaging

R. Ballabriga,[a,1] **J. Alozy,**[a] **G. Blaj,**[a] **M. Campbell,**[a] **M. Fiederle,**[d] **E. Frojdh,**[a] **E.H.M. Heijne,**[a,b,c] **X. Llopart,**[a] **M. Pichotka,**[d] **S. Procz,**[d] **L. Tlustos**[d] **and W. Wong**[a]

[a] *CERN,*
1211 Geneva, 23, Switzerland
[b] *IEAP-CTU,*
Horská 3a/22, 128 00 Praha 2, Czech Republic
[c] *NIKHEF,*
Science Park 105, 1098 XG Amsterdam, The Netherlands
[d] *Freiburger Materialforschungszentrum FMF, Albert-Ludwigs-Universität*
Stefan-Meier-Straße 21, D-79104 Freiburg, Germany

E-mail: rafael.ballabriga@cern.ch

ABSTRACT: The Medipix3 chips have been designed to permit spectroscopic imaging in highly segmented hybrid pixel detectors. Spectral degradation due to charge sharing in the sensor has been addressed by means of an architecture in which adjacent pixels communicate in the analog and digital domains on an event-by-event basis to reconstruct the deposited charge in a neighbourhood prior to the assignation of the hit to a single pixel. The Medipix3RX chip architecture is presented. The first results for the characterization of the chip with 300 μm thick Si sensors are given. $\sim$72e$^-$ r.m.s. noise and $\sim$40e$^-$ r.m.s. of threshold dispersion after chip equalization have been measured in Single Pixel Mode of operation. The homogeneity of the image in Charge Summing mode is comparable to the Single Pixel Mode image. This demonstrates both modes are suitable for X-ray imaging applications.

KEYWORDS: Analogue electronic circuits; Electronic detector readout concepts (solid-state); Digital electronic circuits

[1] Corresponding author.

doi:10.1088/1748-0221/8/02/C02016

Contents

2013 JINST 8 C02016

1 Introduction

Hybrid pixel detectors open up possibilities in many fields of science. Modern High Energy Physics experiments use hybrid pixel detectors for tracking systems where excellent spatial resolution, precise time tagging and high signal-to-noise ratio are required for accurate track reconstruction [1–3]. Many groups are working worldwide to adapt hybrid pixel technology to other fields of science such as medical X-ray radiography [4–7], protein crystallography [8–10], adaptive optics [11] or neutron imaging [12, 13] among others.

Two previous generations of the Medipix chip have been designed and tested. The Medipix1 [14] demonstrated the principle of the photon counting approach. The chip was implemented in a 1 μm CMOS process and consisted of a matrix of 64×64 pixels. The pixel dimensions were $170\,\mu\text{m} \times 170\,\mu\text{m}$. The Medipix2 chip [15] was implemented in a 0.25 μm CMOS technology with a matrix of 256×256 pixels. The pixel dimensions were $55\,\mu\text{m} \times 55\,\mu\text{m}$.

In conventional highly segmented pixel detectors such as Medipix2 there is a limitation when measuring the energy of a single photon. This technological limitation comes from the distortion in the energy spectrum measured by one pixel induced by charge sharing. When a photon deposits its energy in the semiconductor detector material, the generated electron-hole cloud drifts under the electric field but also diffuses. When the photon deposition takes place in the vicinity of the pixel edges, some signal is induced in the neighbouring pixels. The charge generated in a photon interaction is "shared" between pixels. This produces a distortion in the energy spectrum measured by the individual pixels. This effect is more pronounced when the sensor thickness increases with respect to the pixel pitch. Depending on the programmed threshold on the pixel, a single photon

can be counted in more than one pixel or missed. The pixel-to-pixel threshold dispersion present in the read out chip will also affect the measurement leading to fixed pattern noise in the image.

When using high-Z sensor materials, to increase the detective quantum efficiency at higher photon energies, fluorescence photons can be produced and they deposit their energy at some distance (in the order of tens of micrometres) with respect to the initial photon deposition. The distances involved are comparable to the pixel pitch. Fluorescence photons also affect the energy spectrum measured by the pixel because a fraction of the energy of the original photon, carried by the fluorescence photon, is deposited in an adjacent pixel with respect to the location of the original deposition.

The Medipix3 chips have been designed to permit spectroscopic imaging in highly segmented hybrid pixel detectors. Spectral degradation due to charge sharing in the sensor has been addressed by means of an architecture in which adjacent pixels communicate in the analog and digital domains on an event-by-event basis to reconstruct the deposited charge in a neighbourhood prior to the assignation of the hit to a single pixel. Applications based on spectroscopic techniques will benefit from this approach. Those include example k-edge imaging, X-ray fluorescence spectroscopy or spectroscopic CT imaging.

In the first version of the Medipix3 chip ([16, 17]) the charge sharing tail was properly cancelled by the summing circuit but the hit allocation mechanism worked poorly due to an unexpectedly high pixel-to-pixel threshold mismatch and an architecture sensitive to it. The new chip, the Medipix3RX, implements a new architecture for the hit allocation which works well in simulations [18] and which is more robust to pixel-to-pixel threshold mismatch. This contribution describes the new chip architecture and the first results obtained.

Sections 2 and 3 describe the Medipix3RX readout chip and the pixel architecture. Section 4 describes the results of the first measurements on Medipix3RX readout chips bump bonded to 300 μm thick silicon sensors. Finally, spectroscopic imaging in highly segmented hybrid pixel detectors is demonstrated in an experiment where material analysis is performed analysing the energy dependent absorption properties of different materials.

2 Chip description

The Medipix3RX in its usual form measures 15.9×14.1 mm and has been designed using a commercial 0.13 μm CMOS technology with 8 metal layers. Figure 1 shows a photo of the Medipix3RX chip.

The sensitive area contains a 256×256 matrix of 55 μm square pixels. The chip can be tiled on three sides.

The periphery at the bottom of the chip contains synchronous IO logic with a command decoder, various analog blocks, 32 electrically programmable and readable fuses for chip identification, 8 IO LVDS transceivers and a large number of power pads.

The analog periphery block contains a band-gap voltage reference with on-chip temperature sensor, 27 DACs (10 9-bit DACs and 17 8-bit DACs) and 2 independent test pulse circuits per pixel column. The width of the IO parallel data port is configurable using either 1, 2, 4 or 8 LVDS lines. Region of interest readout is also possible by selecting either 32, 64 or 128 column blocks and/or a number of rows to be read out.

2013 JINST 8 C02016

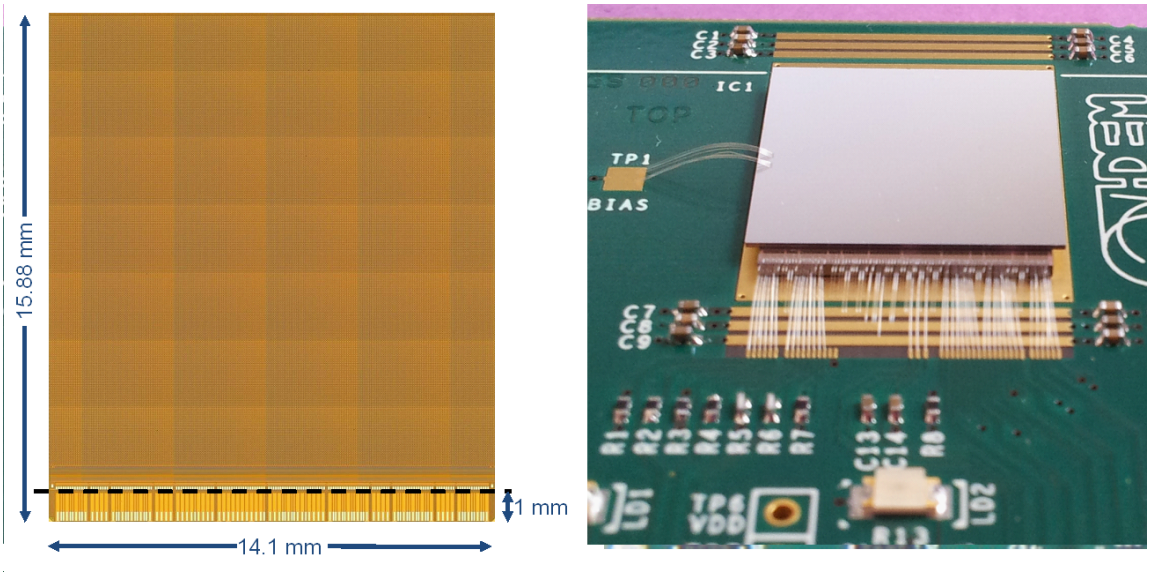

Figure 1. On the left hand side, the picture of the Medipix3RX chip is shown. On the right hand side, the chip connected to a 300 μm thick Si sensor is shown.

The chip IO can be connected to a printed circuit board either using standard wire bonding or through-silicon via technology (TSV). Wire bond extenders allow the electrical connection of the chip to a readout card by using standard wire bonding once the sensor is bonded to the active area. The wire bond extenders can be diced (dashed line in figure 1) without compromising the chip functionality. In the case where the wire bond extenders are diced, connection is possible through smaller wire bond pads or through TSVs. Connection through TSV requires further processing of the readout chip wafers. When TSV's are used the die size is reduced to 14.1×14.9 cm^2. The active area represents 94.3 % of the total surface area of the die.

The analog power consumption is around 600 mW in Single Pixel mode and below 900 mW in Charge Summing mode. The average digital power consumption is ~250 mW with a 200 MHz readout clock.

3 Pixel architecture

A diagram illustrating the algorithm designed to mitigate the effects of charge sharing and implemented in the Medipix3RX chip is shown in figure 2. When a photon deposits its energy in the vicinity of the edge of a pixel, due to diffusion of charge, some signal is induced in a cluster of pixels. The charge deposited on a pixel is compared with the charge from its neighbours by means of a network of arbitration circuits that unambiguously allocate the hit to the pixel that had the largest charge deposit (figure 2, left). In parallel to that process, summing circuits physically located at the corners between pixels reconstruct the charge in clusters of 2×2 pixels (figure 2, right). If a pixel has the highest charge deposition with respect to its neighbours and one of the adjacent summing circuits exceeds the programmed threshold then a counter in the pixel is incremented.

The pixel schematic when configured to implement this algorithm is shown in figure 3. The input pad is connected to a preamplifier implemented using the Krummenacher [19] architecture.

2013 JINST 8 C02016

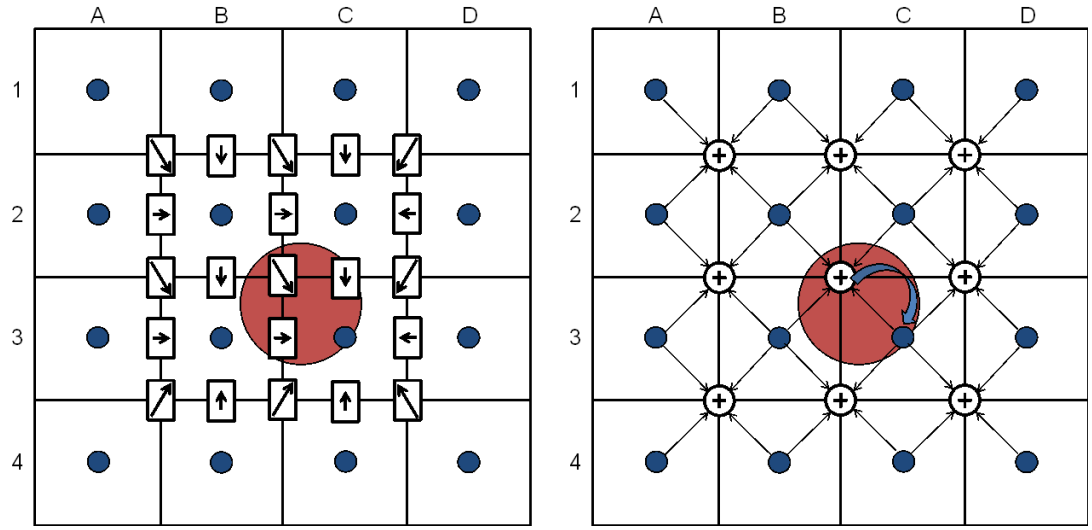

Figure 2. Illustration of the Charge Summing Algorithm. The local charge deposited in the semiconductor detector material by a single event is compared with a threshold. The output of the comparator is fed into an arbitration network to determine which pixel received the largest charge (left). A counter in the pixel with the largest charge deposited increases if the reconstructed charge in one of its neighbouring summing circuits exceeds the programmed threshold.

The value of the feedback capacitance is selectable between 7fF for the highest gain, 14fF, 21fF and 28fF for the lowest gain. The preamplifier can handle both positive and negative charges. A test injection capacitance is provided in each pixel in order to permit full testing of the chip functionality using electrical stimuli. 2 different test pulses are available on the chip to allow injection of different charges in adjacent pixels.

The output of the charge sensitive amplifier is processed by a first order semi-gaussian shaper which has a time constant of $\sim$120ns. The shaper acts both as a noise filter and as a transconductance, generating five output currents with amplitudes proportional to the induced charge in the input pad. The shaper output currents can be programmed to be connected to different discriminators depending on the programmed mode of operation.

The pixel can be programmed in "Single Pixel Mode" or in "Charge Summing Mode". In "Single Pixel Mode", the shaper outputs are connected to the local discriminators and the arbitration and synchronization logic are inhibited. The pixels in this mode of operation are independent with respect to their neighbouring pixels.

In "Charge Summing Mode" one of the currents is compared to a threshold (TH0) by means of a discriminator. The four other currents are sent to the adjacent summing nodes where they are combined with the signals from the adjacent pixels in order for the charge reconstruction to be done. The reconstructed signal is compared to a threshold (TH1) by means of a discriminator. Each of the two discriminators on the pixel contains a 5-bit DAC to digitally correct for the pixel-to-pixel threshold mismatch.

The arbitration logic compares the local signal with the signal in the adjacent pixels and if the local pixel has the largest energy deposit then counter 0 is incremented. The counter 0 elements of the adjacent pixels are inhibited from incrementing for the same photon. The decision of the

2013 JINST 8 C02016

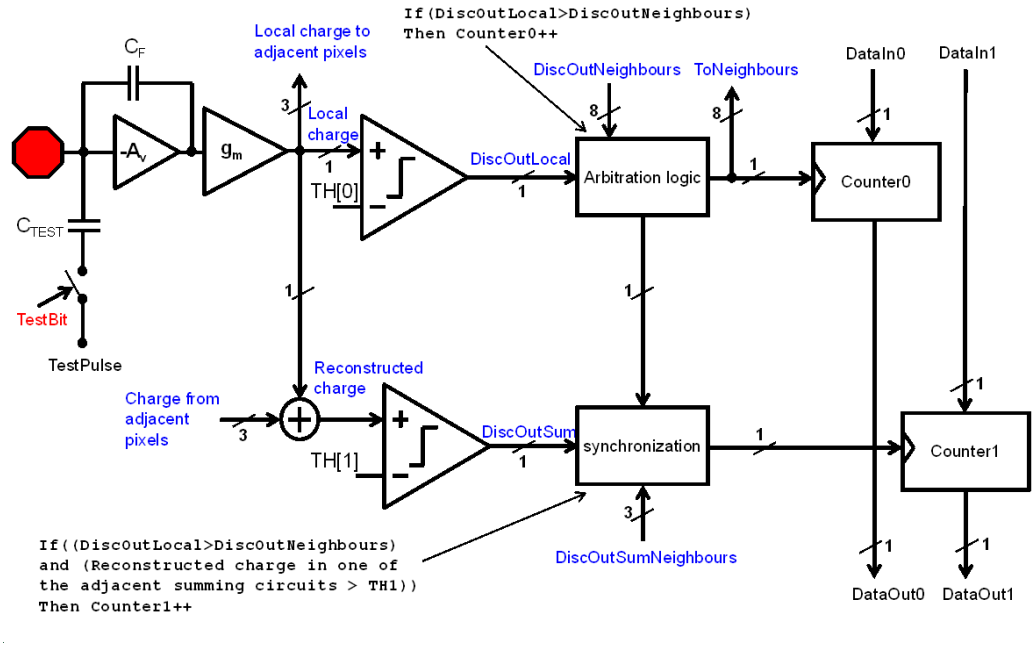

Figure 3. Schematic block diagram of the pixel when configured in Charge Summing Mode.

arbitration logic is based on the timing properties of the discriminator output signal. This channel is named "single pixel mode arbitrated" because a threshold is applied to the local signal and the arbitration circuitry is used to suppress the hit from the pixels with lower signal.

In parallel to the process of allocating the hit, the charge is reconstructed in the summing circuits. The synchronization logic increases counter 1 if the hit is allocated to the local pixel and the charge reconstructed in one of the adjacent summing circuits exceeds the programmed threshold (TH1). The mode of operation in which the charge is reconstructed and allocated to a single pixel is called "Charge Summing Mode".

The pixel matrix can also be programmed in "Fine Pitch Mode" or in "Spectroscopic Mode". In Fine Pitch Mode, the pitch of the detector pixels matches the 55 μm pitch of the readout chip. In Spectroscopic Mode, the readout pixels are grouped in clusters of four which become a single detector unit. In this case the detector pitch is 110 μm and only one readout pixel in four is bump bonded. When programmed in this mode of operation the circuitry in the pixels that were not bump bonded is used to provide more energy thresholds. In the case of "Spectroscopic Mode" with "Single Pixel Mode" the number of thresholds available is 8. In this situation the clusters are independent of their neighbours. In the case of "Spectroscopic Mode" with "Charge Summing", 4 thresholds in which the charge reconstruction algorithm is applied at a cluster level are available. 4 other thresholds with the local deposited charge information are available in this mode (see figure 1).

There are two Linear Feedback Shift Registers per pixel which can be configured as counters with overflow control (the full counter range is available) during data acquisition or as shift registers during chip readout. They can be configured as 2×1-bit counters, 2×6-bit counters, 2×12-bit counters or 1×24-bit counter.

2013 JINST 8 C02016

Table 1. Chip configuration modes.

Matrix configuration	**Pixel Operating Modes**	**Thresholds**
Fine Pitch Mode (55µm)	Single Pixel Mode	2
	Charge Summing Mode	1+1
Spectroscopic Mode (110µm)	Single Cluster Mode	8
	Charge Summing Mode	4+4
Front-end gain mode	**Linearity**	**Thresholds**
Super High Gain Mode	~5 ke^-	2
High Gain Mode	~9 ke^-	
Low Gain Mode	~12.5 ke^-	
Super Low Gain Mode	~18 ke^-	
Pixel Counter Modes	**Dynamic range**	**Counters**
1-bit	1	2
6-bit	63	2
12-bit	4095	2
24-bit	16777215	1
Pixel readout mode	**Active Counters**	**Dead Time**
Sequential Read-Write	2	Yes
Continuous Read-Write	1	No

If dead time free operation is desired, the chip can be programmed in "Continuous Read Write". In this mode of operation one counter is incremented while the other is being read out. The threshold to be read out is selectable. The digital circuitry of the pixel matrix was implemented using standard digital design flow using a high density digital library using low power transistors. Previous designs of the Medipix family of chips had been designed with full custom digital layout.

The regular structure in the matrix is shown in figure 4. It consists of a 2×2 pixel cluster. The digital circuitry of pixels 1–2 and 3–4 are merged in order to share common circuitry and minimize the circuit area. The analog circuitry was designed with emphasis of best layout practices for matching.

4 Measurements

4.1 Gain, noise and threshold dispersion

The gain, noise and threshold dispersion were characterized in Medipix3RX chips bump-bonded to 300 μm thick Silicon sensors. The Fitpix readout system [20] from IEAP Prague was used along with a specially modified version of the Pixelman software [21]. The measurements of gain, noise and threshold dispersion were done using the electrical test pulse and the s-curve method [22]. The measurement of electrical parameters using the injection of test pulses relies on the knowledge of the value of the test capacitance which depends on technology parameters and which can have a tolerance of $\pm 20\%$ with respect to the nominal design value (this capacitance is shown in the

2013 JINST 8 C02016

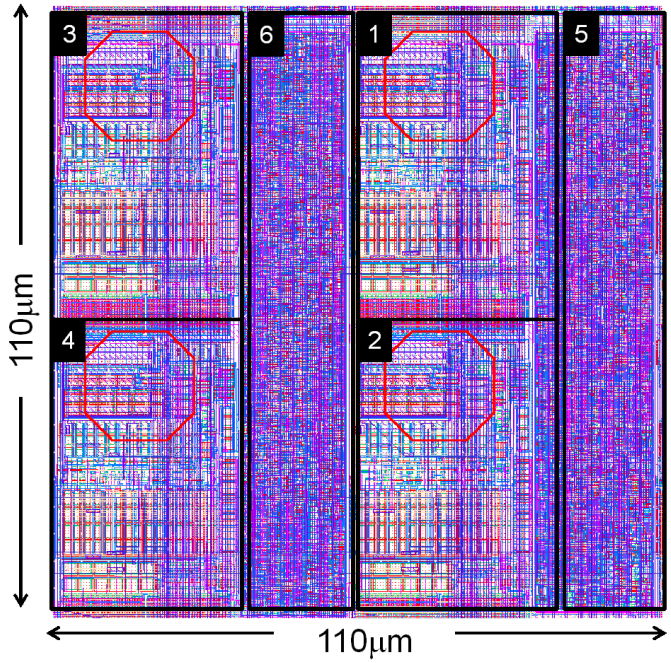

Figure 4. Layout of the regular structure in the pixel matrix. The regular structure is a cluster of 2×2 pixels ($110\,\mu\text{m} \times 110\,\mu\text{m}$). 1–4 shows the analog circuitry of pixels one to four. 5 and 6 show the digital circuitry of pixels 1–2 and 3–4 respectively. The digital circuitry of two pixels was merged in order to share resources between pixels.

Table 2. Gain, noise and threshold dispersion parameters for the low power operating point (Ipreamp=60, Ishaper=90).

Gain Mode	Mode	Gain (e^-/DAC step)	ENC (e^- r.m.s.)	Threshold dispersion (e^- r.m.s.)
SHGM	SPM	37	86	55.5
	CSM	77	203	115.5
HGM	SPM	66	95	99
	CSM	142	200	213
LGM	SPM	94	106	141
	CSM	207	219	310
SLGM	SPM	123	119	184
	CSM	279	247	418

schematic in figure 3 (C_{TEST})). The total charge injected in the preamplifier is proportional to the amplitude of the square wave (TestPulse in figure 3) and to the value of the test capacitance.

In order to provide an accurate measurement of the front-end parameters, the value of the test capacitance was extracted from measurements with radiation sources. Table 2 and table 3, summarize the results of the gain (expressed in electrons at the preamplifier input per threshold DAC step), the equivalent noise charge in e^- r.m.s. and the threshold dispersion (expressed in e^- r.m.s.) of the front-end for the different modes of operation.

The energy spectrum shown in the chip was measured for a ^{109}Cd source in the Single Pixel Mode and in Charge Summing Mode of operation. Before measuring, the pixel matrix was equal-

Table 3. Gain, noise and threshold dispersion parameters for the low noise operating point (Ipreamp=250, Ishaper=200).

Gain Mode	Mode	Gain (e^-/DAC step)	ENC (e^- r.m.s.)	Threshold dispersion (e^- r.m.s.)
SHGM	SPM	25	72	37.5
	CSM	57	148	85.5
HGM	SPM	45	80	67.5
	CSM	107	174	160.5
LGM	SPM	65	93	97.5
	CSM	155	201	232.5
SLGM	SPM	87	107	130.5
	CSM	207	233	310.5

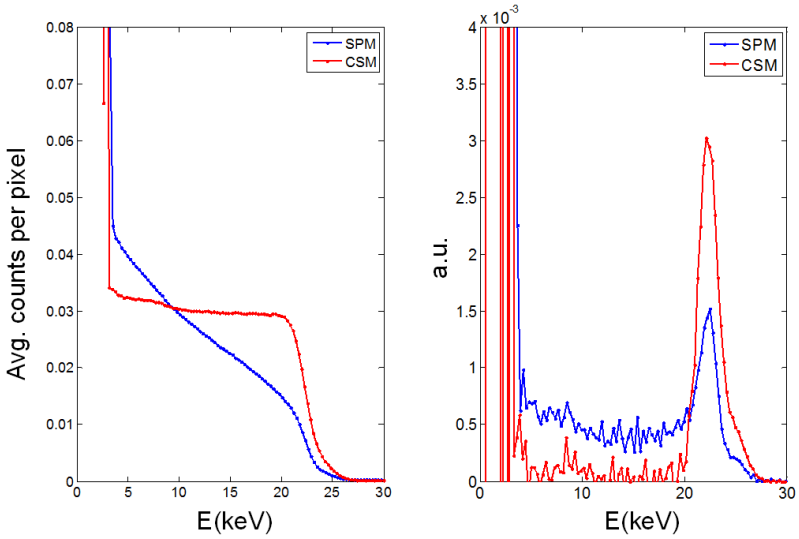

Figure 5. Measurement of the energy spectrum of a ^{109}Cd source. (left) Threshold scan data showing the average number of counts per pixel at each threshold step. (right) Energy spectrum (differentiation of the plot at the left). The chip was equalized and only 4 pixels were masked in the full matrix. No pixel realignment was applied to the data.

ized. Only 5 pixels were masked for this measurement. The results are shown in figure 5. The energy spectrum when the pixel is programmed in single pixel mode presents a distortion for low energies. The by means of applying the charge summing algorithm the charge sharing tail is eliminated.

4.2 Imaging

Some X-ray images were taken to study the impact of the new architecture on the image quality. Figure 6 shows two contrast images of a Line Pair per Millimeter phantom. On the left hand side the image is shown for the chip programmed in Single Pixel Mode. The arbitration circuitry is inhibited in this case. On the right hand side the raw contrast image in charge summing is shown. Note the homogeneity in the charge summing mode image is comparable to the single pixel mode image. This demonstrates that both modes of the Medipix3RX are suitable for X-ray imaging applications.

2013 JINST 8 C02016

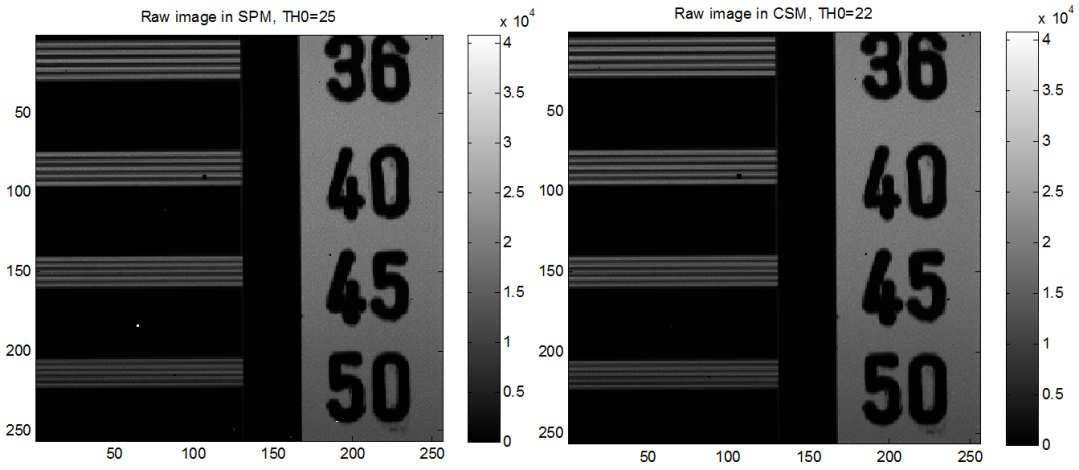

Figure 6. Raw images of a LPPM phantom in Single Pixel Mode (left) and in CSM (right). Cu X-ray tube at 15kV and 5mA, 2mm Al filtering, 1 second acquisition.

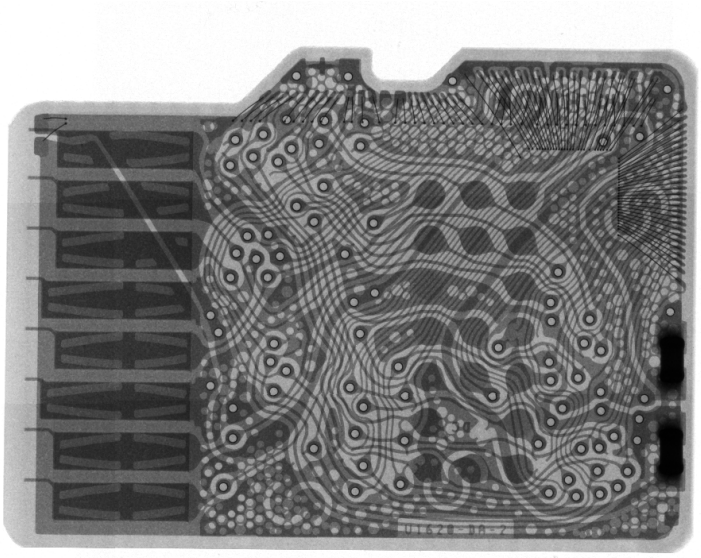

Figure 7. X-ray image in CSM of a micro-SD card. Image consists of 4×3 single tiles, the geometrical magnification is $3.2\times$. X-ray tube at 30 kVp, 100 μA and 1mm Al-filtering. 5 seconds acquisition per tile.

Figure 7 shows the image of a micro-SD card measured in charge summing mode. The Medipix3RX detector was scanned for this image to provide a larger detection area. A total of 12 single acquisitions were used to achieve an image with 3.2x geometrical magnification and 1024×768 pixels. The resulting object resolution is 17 μm here. An X-ray tube with tungsten anode, 5 μm focus diameter, 30 kVp and 1mm Al-filtering was used for this measurement. A flat field correction was applied without further post processing. The routing of the conducting paths inside the card is clearly visible.

2013 JINST 8 C02016

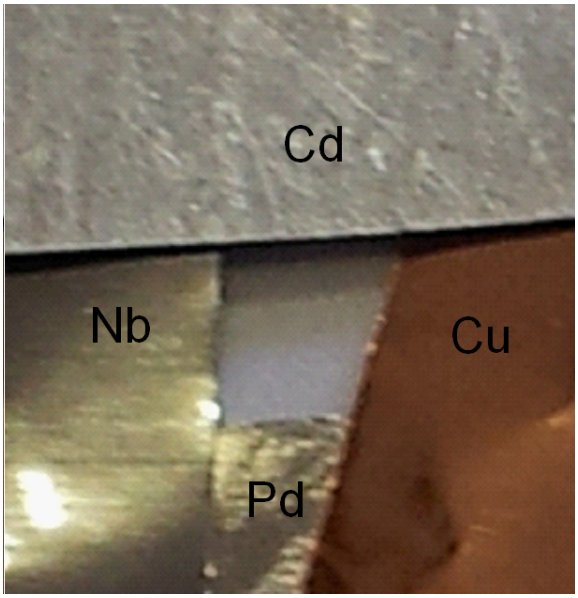

Figure 8. Sample, 4 partially overlapping metal foils.

4.3 K-edge imaging

The Medipix3 chips were designed to allow spectroscopic imaging for highly segmented hybrid pixel detectors by eliminating the charge sharing distortion in the measured pixel energy spectrum. This section presents the results of the first measurements in an experiment aimed at distinguishing between four different materials by identifying their energy dependent absorption coefficient.

4.4 Measurement setup

The X-ray measuring setup constructed at the Freiburger Materialforschungszentrum (FMF) is described elsewhere [23]. A Hamamatsu L10101 X-ray tube (with a tungsten anode and 150 μ thick beryllium window) at 50 kV and 200 μA provided the initial spectrum. This spectrum was filtered with a 2 mm aluminium filter placed directly on the X-ray tube in order to optimize the ratio between the different energies used in this study (13.5–35 keV). The detector was a Medipix3RX chip bump-bonded to a 300 μm silicon sensor with a bias voltage of 90 V. The threshold equalization mask was generated using the noise floor.

The sample consisted of a superposition of four metallic foils (Cu, Nb, Pd and Cd with thicknesses in the order of tens of micrometres) along the sides of the detector, overlapping at the corners and leaving a direct beam area in the centre (figure 8). These regions were numbered from 1 to 9 for identification.

The sample was mounted at 25 cm from the X-ray tube and the detector at a distance of 25 cm from the sample, in order to minimize scattering and sample fluorescence effects on the measured spectra.

All measurements were performed in Charge Summing Mode, using a single threshold and acquiring frames sequentially at each threshold setting. We acquired frames with minimum energy thresholds of 35 to 100 with a step of 1 (nominally corresponding to energy thresholds 12.5–45 keV

2013 JINST 8 C02016

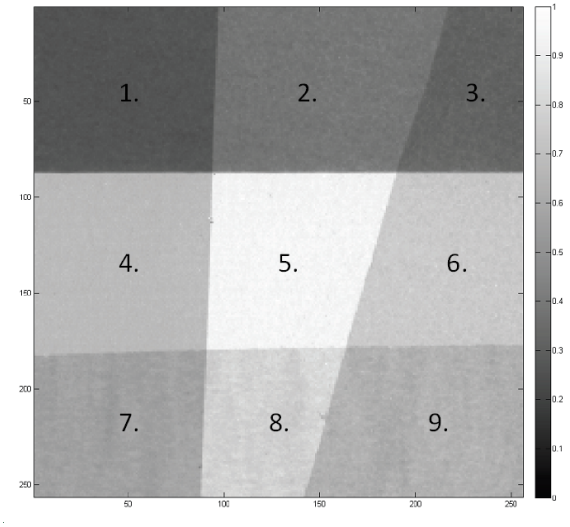

Figure 9. X-ray image measured in absorption and normalized by the flat field. Region 5 represents the direct beam. Regions 2, 4, 6 and 8 represent non-overlapping metal foils. Regions 1, 3, 7 and 9 represent overlapping metal foils.

in steps of 0.5 keV). In subsequent analysis we only used measurements in the range 13.5–35 keV. Each frame thus contains counts for detected photons with energies between the threshold setting and infinity.

While looping over the threshold settings, we acquired 40 frames for each sample image. After measuring the sample, we measured the flat field (direct beam without sample) by acquiring 10 frames.

4.5 Results

Figure 9 shows the typical x-ray imaging result when no spectroscopic information is collected. Note that the unidimensional (grayscale) result makes it impossible to distinguish between the absorption of different materials and the absorption of different thicknesses.

For extracting the spectral information, the raw sample spectra were calculated for each pixel and energy bin by subtracting the number of counts obtained with the corresponding high energy threshold from the corresponding low energy threshold. The raw flat field spectrum was calculated similarly from the flat field measurements. Normalizing the raw sample spectra by the flat field spectrum provides the transmission for each pixel and each energy bin on a scale from 0 to 1.

For regions 2, 4, 6 and 8 (non-overlapping foils), the median spectra were calculated by selecting the median value for each region and each energy bin (figure 10). The materials can be identified: Cu has no absorption edge in this region, thus it corresponds to the blue dots. The identification of Nb, Pd and Cd is also straightforward and in concordance with the energies of absorption edges (18.984 keV, 24.351 keV and 26.712 keV respectively).

Figure 10 compares the measured transmission spectra with the spectra calculated theoretically using the linear attenuation coefficients from [24] and fitting the materials thicknesses. The measured spectra (dots) and simulated (lines) are in excellent agreement. Note that the apparently

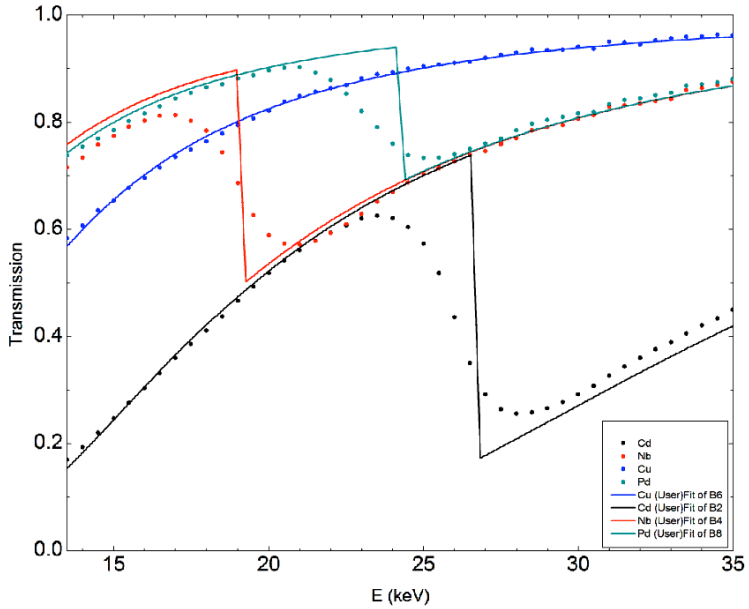

Figure 10. Dots represent the spectroscopic information corresponding to regions 2, 4, 6 and 8 (non-overlapping metal foils). They represent measured data, obtained by using the transmission for each energy bin and averaged on all the pixels in the corresponding region. The Cu foil transmission spectrum is continuously increasing with energy, while the absorption edges of Nb, Pd and Cd foils are clearly visible. The lines represent the corresponding transmission spectra calculated theoretically from the linear attenuation coefficients in their respective materials and fitting the thickness of each material. Note that the apparently gradual change in measured transmission spectra around absorption edges is due to the detection energy resolution and the effect of averaging multiple pixel spectra.

gradual change in measured transmission spectra around absorption edges is due to the detection energy resolution and the effect of averaging multiple pixel spectra which are not perfectly aligned.

While sequentially measuring full spectra can be useful, it is also relatively time consuming. By choosing only 3 energy bins (delimitated by 4 thresholds) we are still able to distinguish the materials with absorption edges (figure 11).

In figure 11 (left), the color of each pixel is given by a RGB (red green blue) code where the red, green and blue channels represent the transmission in the energy bins 13.5–19 keV, 19–24 keV and 24–26 keV respectively. The 19, 24 and 26 keV thresholds correspond to the Nb, Pd and Cd absorption edge energies.

While blue tints are generally expected due to increasing transmission at higher energies (due to "beam hardening"), the presence of an absorption edge between two energy bins will cause sharp colors (more intense blue shades, but also other colors like red and green in this color representation). The red band can be identified immediately as Nb and the green band as Pd. Cu is blue (no absorption edge), and Cd is also blue (energy bin above absorption edge outside displayed range).

Figure 11 (right) is similar to figure 11 (left). The only difference is that the red, green and blue channels are mapped to the transmission in the energy bins 19–24 keV, 24–26 keV and 26–35 keV. In this representation, the Nb transition edge is not visible anymore (energy bin under absorption edge outside displayed range), thus its color (red in 5 A) becomes blue (typical for beam hardening

2013 JINST 8 C02016

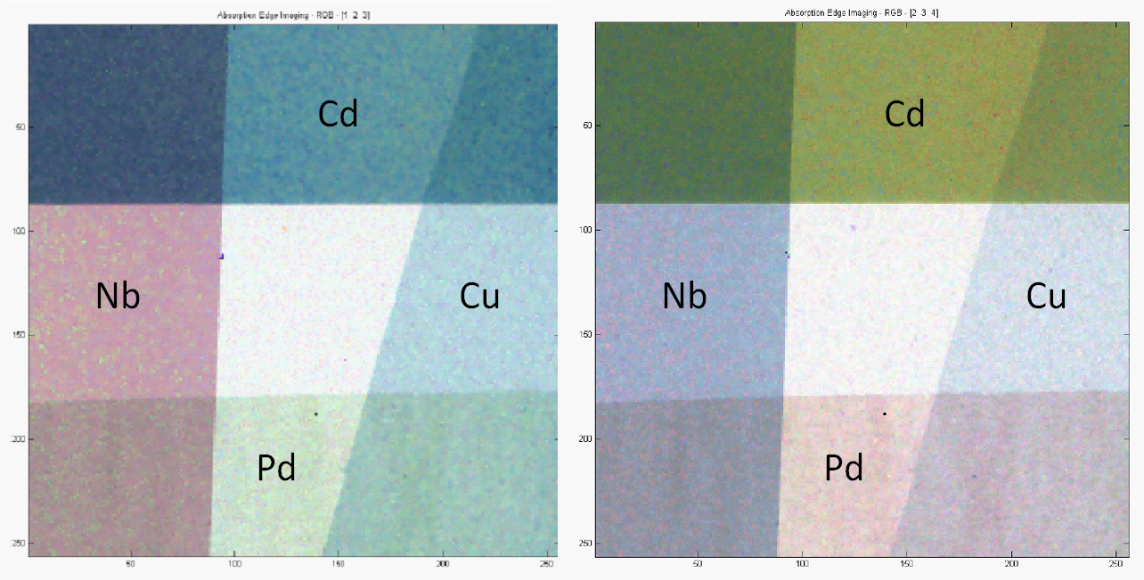

Figure 11. Spectroscopic imaging using only 3 energy bins delimited by 4 energy thresholds. The picture on the left hand side displays in the red, green and blue channels the transmission in the energy bins 13.5–19 keV, 19–24 keV and 24–26 keV respectively. The picture on the right hand side displays in the red, green and blue channels the transmission in the energy bins 19–24 keV, 24–26 keV and 26–35 keV. While blue tints are generally expected due to increasing transmission at higher energies, the presence of an absorption edge between two energy bins will cause sharp colors. Careful analysis of the colors allow the identification of regions 2, 4, 6 and 8 as Cd, Nb, Cu and Pd.

but no visible absorption edge). The absorption edge of Pd moves by one bin (from green in figure 11 (left)) to red. The absorption edge of Cd becomes visible (green). Cu remains blue (no absorption edge).

While sequential measurements with many energy bins are very flexible, allowing precise identification of elements based on absorption spectroscopy, in some applications the measurement time can be dramatically decreased by using only 4–8 energy thresholds simultaneously (possible in the spectroscopic mode of Medipix3RX, in combination with the Charge Summing Mode algorithm). Additionally, simultaneous measurements reduce the noise due to quantum effects (poisson distribution of the number of counts when repeating measurements) by comparing the energy of each detected photon against different thresholds simultaneously.

Even if the absorption edges of different elements are close (similar to the example presented here, with Pd and Cd), these can be discriminated easily by setting some of the detection thresholds on the absorption edge energies. Arguably, this functionality would be extremely useful in, e.g., medical imaging applications using contrast agents.

5 Conclusion

The Medipix3RX chip implements in hardware an algorithm permitting spectroscopic imaging with high spatial resolution for hybrid pixel detectors. The Medipix3RX has successfully corrected the limitations the Medipix3.0.

2013 JINST 8 C02016

$\sim 72e^-$ r.m.s. noise and $40e^-$ r.m.s. of threshold dispersion after chip equalization have been measured in Single Pixel Mode of operation. The homogeneity of the image in Charge Summing mode is comparable to the Single Pixel Mode image. This demonstrates both modes are suitable for X-ray imaging applications.

The measurements presented in the manuscript show how the charge sharing tail is removed from the energy measurement when the chip is programmed in charge summing mode. Applications in which spectroscopy at a pixel level is necessary will benefit from this implementation, for example, material analysis using X-rays of spectroscopic computed tomography.

Acknowledgments

The authors would like to thank the Medipix2 and 3 collaborations. The authors would also like to thank H. Tuinhout, M. Vertregt and M. Pelgrom for their advice on matching and E. Miranda for discussions on oxide reliability and random telegraphic signals.

References

[1] ALICE SILICON PIXEL DETECTOR PROJECT collaboration, P. Riedler et al., *Operation and performance of the ALICE silicon pixel detector with proton-proton beams*, *Nucl. Instr. Meth.* **A 650** (2011) 6 [ISSN 0168-9002].

[2] G. Gagliardi, *The ATLAS Pixel Detector: A hundred million channels vertex detector for LHC*, *Nucl. Instr. Meth.* **A 546** (2005) 67.

[3] R. Baur and W. Bertla, *The CMS pixel vertex detector*, *Nucl. Phys. B Proc. Supp.* **78** (1999) 293.

[4] A. Butler et al., *Bio-medical X-ray imaging with spectroscopic pixel detectors*, *Nucl. Instrum. Meth.* **A 591** (2008) 141.

[5] M. Firsching, A. P. Butler, N. Scott, N. G. Anderson, T. Michel and G. Anton, *Contrast agent recognition in small animal CT using the Medipix2 detector*, *Nucl. Instr. Meth.* **A 607** (2009) 179.

[6] M.G. Bisogni et al., *A Medipix2-based imaging system for digital mammography with silicon pixel detectors*, *IEEE Trans. Nucl. Sci.* **NS-51** (2004) 3081.

[7] G. Blanchot et al., *Dear-Mama: A photon counting X-ray imaging project for medical applications*, *Nucl. Instr. Meth.* **A 569** (2006) 136.

[8] C. Ponchut, J. Clement, J.M. Rigal et al., *Photon-counting X-ray imaging at kilohertz frame rates*, *Nucl. Instr. Meth.* **A 576** (2007) 109.

[9] B. Henrich et al., *PILATUS: A single photon counting pixel detector for X-ray applications*, *Nucl. Instr. Meth.* **A 607** (2009) 247.

[10] P. Pangaud et al., *XPAD3: a new photon counting chip for X-ray CT-scanner*, *Nucl. Instr. Meth.* **A 571** (2007) 321.

[11] J. Vallerga, J. McPhate, A. Tremsin, O. Siegmund, B. Mikulec and A. Clark, *Optically sensitive Medipix2 detector for adaptive optics wavefront sensing*, *Nucl. Instr. Meth.* **A 546** (2005) 263.

[12] J. Jakubek et al., *Neutron Imaging with MEDIPIX2 Chip and a Coated Sensor*, *Nucl. Instr. Meth.* **A 560** (2006) 143.

2013 JINST 8 C02016

[13] A.S. Tremsin et al., *On the possibility to image thermal and cold neutron with sub-15 μm spatial resolution*, *Nucl. Instr. Meth.* **A 592** (2008) 374.

[14] M. Campbell, E.H.M. Heijne, G. Meddeler, E. Pernigotti and W. Snoeys, *Readout for a* 64×64 *Pixel Matrix with 15-bit Single Photon Counting*, *IEEE Trans. Nucl. Sci.* **45** (1998) 751.

[15] X. Llopart, M. Campbell, R. Dinapoli, D. San Segundo and E. Pernigotti, *Medipix2: a 64-k Pixel Readout Chip With 55-mm Square Elements Working in Single Photon Counting Mode*, *IEEE Trans. Nucl. Sci.* **49** (2002) 5.

[16] X. Llopart, R. Ballabriga, M. Campbell, E. Heijne, L. Tlustos, W. Wong, Nucl. Instrum. Methods Phys. Res., A 633 (2011) S15-S18.

[17] R. Ballabriga, *The Design and Implementation in 0.13 μm of an Algorithm Permitting Spectroscopic Imaging with High Spatial Resolution for Hybrid Pixel Detectors*, Ph.D. Thesis, Universitat Ramon Llull (2009).

[18] D. Pennicard, R. Ballabriga, X. Llopart, M. Campbell and H. Graafsma, *Simulations of charge summing and threshold dispersion effects in Medipix3*, *Nucl. Instr. Meth.* **A 636** (2011) 74.

[19] F. Krummenacher, *Pixel Detectors with Local Intelligence: an IC Designer Point of View*, *Nucl. Instr. Meth.* **A 305** (1991) 527.

[20] V. Kraus, M. Holik, J. Jakubek, M. Kroupa, P. Soukup and Z. Vykydal, *FITPix — Fast Interface for Timepix Pixel Detectors*, 2011 *JINST* **6** C01079.

[21] D. Turecek, T. Holy, J. Jakubek, S. Pospisil and Z. Vykydal, *Pixelman: a multi-platform data acquisition and processing software package for Medipix2, Timepix and Medipix3 detectors*, 2011 *JINST* **6** C01046.

[22] F. Anghinolfi et al., *A 1006 element hybrid silicon pixel detector with strobed binary output*, *IEEE Trans. Nucl. Sci.* **NS-39** (1992) 654.

[23] S. Procz et al., *Flatfield correction optimization for energy selective X-ray imaging with Medipix3*, *IEEE Trans. Nucl. Sci.* **58** (2011) 3182.

[24] R.D. Deslattes et al., *X-ray transition energies, NIST Standard Reference Database 128* (2005), available online at http://www.nist.gov/pml/data/xraytrans/index.cfm.

[25] C.T. Chantler et al., *X-ray form factor, attenuation, and scattering tables, NIST Standard Reference Database 66* (2005), available online at http://www.nist.gov/pml/data/ffast/index.cfm

2013 JINST 8 C02016